

Quantized topological states and parity anomaly in intrinsic quantum anomalous Hall insulator MnBi₂Te₄

Zhongxun Guo^{1,2,3,4,5†}, Jingjing Gao^{1,2,3,4,5†*}, Zhiwei Huang^{1,2,3,4,5}, Di Yue^{1,2,3,4,5}, Zhaochen Liu^{1,2}, Mingyan Luo^{1,2,3,4,5}, Shuang Wu^{1,2}, Xinyu Chen^{1,2}, Guangyi Huang¹, Yujun Deng^{1,2,3,4,5}, Mengzhu Shi⁶, Yin Xia¹¹, Zihan Xu⁷, Chuanying Xi⁸, Guangli Kuang⁸, Changlin Zheng¹, Shiwei Wu^{1,2}, Hua Jiang⁹, X. C. Xie^{9,10}, Wenzhong Bao¹¹, Yuping Sun^{8,12,13}, Xian Hui Chen^{6*}, Jing Wang^{1,2*}, Wei Ruan^{1,2,3,4,5*}, Yuanbo Zhang^{1,2,3,4,5,14*}

¹*State Key Laboratory of Surface Physics and Department of Physics, Fudan University, Shanghai 200438, China*

²*Institute for Nanoelectronic Devices and Quantum Computing, Fudan University, Shanghai 200433, China*

³*Shanghai Branch, Hefei National Laboratory, Shanghai 201315, China*

⁴*Shanghai Research Center for Quantum Sciences, Shanghai 201315, China*

⁵*Zhangjiang Fudan International Innovation Center, Fudan University, Shanghai 201210, China*

⁶*Hefei National Laboratory for Physical Science at Microscale and Department of Physics, University of Science and Technology of China, and Key Laboratory of Strongly-coupled Quantum Matter Physics, Chinese Academy of Sciences, Hefei, Anhui 230026, China.*

⁷*SixCarbon Technology, Youmagang Industry Park, Shenzhen 518106, China.*

⁸*Anhui Province Key Laboratory of Low-Energy Quantum Materials and Devices, High Magnetic Field Laboratory, HFIPS, Chinese Academy of Sciences, Hefei 230031, China*

⁹*Interdisciplinary Center for Theoretical Physics and Information Sciences, Fudan University, Shanghai 200433, China*

¹⁰*International Center for Quantum Materials, School of Physics, Peking University, Beijing 100871, China;*

¹¹*School of Microelectronics, Fudan University, Shanghai, 200433, China*

¹²*Key Laboratory of Materials Physics, Institute of Solid State Physics, Chinese Academy of Sciences, Hefei, China.*

¹³*Collaborative Innovation Center of Advanced Microstructures, Nanjing University, Nanjing, 210093, China.*

¹⁴*New Cornerstone Science Laboratory, Shenzhen 518054, China*

† These authors contributed equally to this work.

* Correspondence should be addressed to Y.Z. (zhyb@fudan.edu.cn) and W.R. (weiruan@fudan.edu.cn), J.W. (wjingphys@fudan.edu.cn), X.H.C. (chenxh@ustc.edu.cn) J.G. (gaojj@fudan.edu.cn)

When thinned down to just a few atomic layers, the layered magnetic topological insulator MnBi_2Te_4 offers an exceptional platform for exploring a wide range of topological phenomena^{1–14}. In this work, we overcome longstanding challenges in synthesizing high-purity MnBi_2Te_4 crystals and report the observation of a myriad of quantized topological states in high-quality five-septuple-layer (5-SL) samples under magnetic fields up to 45 Tesla. We show that the nontrivial topology of 5-SL MnBi_2Te_4 , in the presence of Landau quantization, is governed by a generalized topological index rooted in the parity anomaly of Dirac fermions in (2+1) dimensions^{15–19}. The anomaly manifests as an anomalous Landau level, giving rise to gate-tunable helical edge transport. Our results establish high-quality MnBi_2Te_4 as a robust platform for exploring emergent topological states and for advancing novel quantum device applications.

Over the past four decades, various quantized Hall effects have defined an ever-expanding frontier in condensed matter physics. Conventional quantum Hall effects rely on discrete, magnetic-field-induced Landau levels (LLs), which are essential for achieving exact quantization²⁰. However, as first proposed by F. D. M. Haldane, a net external magnetic field is not always necessary—a system with a nontrivial topological electronic structure can defy the LL paradigm and exhibit quantized Hall conductance even at zero external magnetic field¹⁵. This insight has ultimately led to the experimental observation of the zero-field quantum anomalous Hall (QAH) effect in magnetically doped topological insulators, chromium- and vanadium-doped $(\text{Bi,Sb})_2\text{Te}_3$ ^{21–25}, which open exciting opportunities for compact precision metrology^{26–31}, low-dissipation electronics^{21,32–34}, and the realization of chiral Majorana edge states for topological quantum computing^{35–39}.

Realizing the full potential of the magnetically doped topological insulators, however, remains a significant challenge. The short-ranged exchange interaction between the magnetic dopants requires a high doping level (typically around 15%) to establish long-range magnetic order, but these randomly distributed dopants also act as impurities that degrade the quantum transport in this class of materials. The recent advent of MnBi_2Te_4 ^{1–6}, a topological material with innate magnetic order, raises hope for overcoming this dilemma without the need for magnetic doping or additional band structure engineering^{40–46}. Indeed, zero-field Hall conductance quantization has been achieved at a temperature of $T = 1.4$ K in mechanically exfoliated MnBi_2Te_4 flakes with 5 SLs⁷, and later reproduced in 7-SL flake and epitaxially-grown MnBi_2Te_4 films^{47–49}. Furthermore, theoretical calculations for ideal, pristine MnBi_2Te_4 anticipate a topological energy gap on the order of 88 meV—the highest across all existing QAH systems³⁴. These developments highlight MnBi_2Te_4 's tremendous potential as a platform for exploring exotic topological quantum phenomena and potential applications in topological electronics, while also revealing that sample quality remains a major bottleneck limiting further progress with MnBi_2Te_4 .

In this work, we significantly enhance the quality of MnBi_2Te_4 samples by synthesizing high-purity bulk crystals and optimizing sample fabrication. The improved sample quality is demonstrated by a substantial QAH gap up to 30 K, with its field-dependence allowing us to delineate the magnetic structure in the MnBi_2Te_4 flakes. More importantly, the high sample quality enables the electronic transport to reach the extreme quantum limit under magnetic fields up to 45 T, creating a unique opportunity to probe topological states arising from both Landau level (LL) quantization and intrinsic topological order. Remarkably, we find that the sequence of quantized states observed in our experiment defies conventional LL indexing. Instead, these topological states are characterized by a generalized topological index, a concept fundamentally linked to the parity anomaly of Dirac fermions in (2+1) dimensions^{15–19}.

Through model calculations, we identify an anomalous LL that reflects the parity anomaly under high magnetic fields. These calculations further predict that this anomalous LL supports a distinctive helical edge transport, which we confirm experimentally.

We begin by synthesizing high-purity single crystals of bulk MnBi_2Te_4 using a refined self-flux method. A key finding is that replacing the commonly used quenching process by slow cooling to room temperature effectively suppresses the formation of Mn_{Bi} anti-site defects, yielding high-quality bulk MnBi_2Te_4 crystals (see Methods; the X-ray diffraction (XRD) and transmission electron microscopy (TEM) characterization of the crystals is presented in Supplementary Fig. 1). We then mechanically exfoliate the single crystal into atomically thin flakes and pattern metal contacts on top by evaporating Au/Cr (with typical thickness of 70 nm/2 nm) through stencil masks aligned with the flakes. Finally, we use a sharp tip to trim any excess MnBi_2Te_4 , producing devices with uniform thicknesses and well-defined edges that are suitable for subsequent transport measurements. This study focuses on 5-SL specimens in two device configurations. The first, referred to as ‘‘Type A’’, involves 5-SL MnBi_2Te_4 flakes exfoliated using an Al_2O_3 -assisted method as described in ref.⁵⁰. Here we further streamline the exfoliation process by pressing the Al_2O_3 -coated bulk crystal directly onto a sticky substrate covered with a thin adhesive layer from thermal release tape, eliminating heating steps that would otherwise degrade sample quality⁵¹ (Supplementary Fig. 2). The second device type, ‘‘Type S’’, employs MnBi_2Te_4 5-SL flakes directly exfoliated onto SiO_2/Si wafers. Given the high sensitivity of MnBi_2Te_4 flakes to oxygen and moisture, all fabrication processes are conducted in an argon-filled glove box with O_2 and H_2O levels maintained below 0.1 parts per million to minimize sample degradation.

Fig. 1a presents a schematic of a Type A device, featuring an actual 5-SL MnBi_2Te_4 flake (Device A1) supported on a transparent substrate. The substrate consists of a 50-nm-thick indium tin oxide (ITO) layer and a 100-nm-thick Al_2O_3 layer, sequentially grown on a quartz (1000) wafer using atomic layer deposition (ALD). This fully transparent substrate enables accurate layer identification of MnBi_2Te_4 flakes via transmittance imaging⁷, while the conductive ITO layer functions as a back gate for tuning the carrier density in the flakes. Fig. 1b displays the temperature-dependent longitudinal sample resistance, $R_{xx}(T)$, of four 5-SL Type A devices. As temperature T approaches zero, all $R_{xx}(T)$ curves exhibit a sharp drop, a significant departure from the rapid increase reported in previous devices⁷. The sharp drop signifies the emergence of dissipationless edge transport, indicating a much-enhanced device quality.

Indeed, these devices demonstrate substantially improved QAH quantization. Fig. 1c displays the quantized Hall resistance R_{yx} alongside the vanishing longitudinal resistance R_{xx} , measured in a typical 5-SL Type A device (Device A1) at $T = 1.5$ K as the back-gate voltage V_g tunes the device near the charge neutrality point (CNP) of $V_{\text{CNP}} \approx -20$ V. The quantization of R_{yx} achieves a precision better than 1 part in 10^4 , within our measurement uncertainty after correcting for the systematic errors. The quantization remains within 97% of the unit quantum resistance h/e^2 (where h is the Planck constant and e is the elementary charge) up to $T = 4.0$ K (Fig. 1d upper panel). An external magnetic field induces a sharp ferromagnetic (FM) transition, reversing the sign of R_{yx} . Notably, our improved crystal growth and device fabrication methods yield a $\sim 50\%$ success rate (6 out of 11 devices) for observing the zero-field QAH effect.

The improved device quality is further reflected in the elevated energy scale of the QAH

observed. Specifically, we extract the QAH energy gap ΔE from the slope of a line fit to the Arrhenius plot of thermally-activated R_{xx} , where $R_{xx} \propto \exp(-\Delta E/2k_B T)$, and k_B is the Boltzmann constant. This fit yields a zero-field QAH gap as high as $\Delta E = 29.0$ K (Fig. 1e, Device A1)—three times greater than previously reported for few-layer MnBi_2Te_4 and comparable to the largest gaps obtained across all QAH systems^{7,21–25,40–43,45–48}.

More importantly, measurements of the QAH gap under varying magnetic fields provide key insights into the nature of magnetic transitions in Type A devices. These transitions are evident in the magnetic field dependence of R_{xx} measured at elevated temperatures, as marked by colored ticks in Fig. 1e. Arrhenius plots of R_{xx} yield ΔE as a function of magnetic field $\mu_0 H$, with each magnetic state exhibiting distinct field-dependent behavior (Fig. 1e). At low magnetic fields ($\mu_0 H \leq \mu_0 H_1 = 2.2$ T), the interlayer antiferromagnetic (AFM) state dominates, characterized by a ΔE that decreases linearly with increasing field. The slope of this linear trend corresponds to an effective g -factor of -2.1 , consistent with Zeeman narrowing of the QAH gap as the external magnetic field counteracts the exchange field experienced by electrons near the Fermi level⁵². At high fields, a canted antiferromagnetic (CAFM) state develops at $\mu_0 H_2 \approx 4.8$ T, eventually transitioning to a fully polarized FM state at $\mu_0 H_3 \approx 8.4$ T^{53,54}.

The magnetic state in the intermediate field range, $\mu_0 H_1 < \mu_0 H < \mu_0 H_2$, where ΔE exhibits a peak, is particularly intriguing. While signatures of this state were previously observed in AlO_x -capped few-layer samples^{7,47,49}, it was absent in most other measurements. We attribute this state to the collinear magnetized M3' state predicted by both classical Monte Carlo simulations⁵⁵ and AFM linear-chain models⁴⁷ (Supplementary Fig. 4). This M3' state features significantly enhanced magnetization at both surfaces (Fig. 1e inset), which explains the drastic increase in ΔE . The similarities in both the field-dependent QAH gap behavior and the simulation results between our system and AlO_x -capped 7-SL MBT device⁴⁷ suggest that they share a common magnetic origin. Our simulations further reveal the nominal parameters of MnBi_2Te_4 place the system near a critical point in the magnetic phase diagram, where slight variations in defects and disorder can lead to substantial sample-to-sample differences observed across various experiments^{7,47,49,54,56–58}. Indeed, Type A devices exhibit a similar set of magnetic transitions, albeit at magnetic fields distinct from those in Type S devices (Fig. 1f; see the schematic of Type S devices in Fig. 2c lower inset).

Furthermore, we find that defects and disorder strongly influence the QAH quantization in MnBi_2Te_4 . Specifically, we observe a pronounced anti-correlation between Mn_{Bi} (Mn residing on the Bi site) anti-site defect density and remnant zero-field R_{yx} in Type A devices—higher defect densities correspond to lower remnant R_{yx} (Supplementary Fig. 3). This anti-correlation likely arises from the magnetic moments of Mn_{Bi} ions, which couple antiferromagnetically to the primary Mn layers^{59,60}. A high density of magnetic Mn_{Bi} ions suppresses the total magnetization experienced by the electrons, thereby degrading the QAH quantization. When an external magnetic field aligns the magnetic moments of Mn_{Bi} ions with the majority moments, the total magnetization is effectively enhanced. This mechanism explains the pronounced, linearly increasing background in the field-dependent ΔE below 8 T in earlier samples with relatively low quality⁷.

As a strong external magnetic field polarizes the magnetization of all five SLs, the magnetic states in both Type A and Type S devices converge to the FM state (Fig. 1e and 1f). The strong magnetic field, meanwhile, drives the two-dimensional electrons of the FM state into the

extreme quantum limit, presenting a unique opportunity to probe a topological system in the presence of quantized LLs. Type S devices are particularly suited to this study due to the high mobility of their surface electrons in the FM state, even though zero-field quantization is not observed in these devices. Indeed, a plethora of quantized topological states emerge as the carrier concentration is modulated under strong magnetic fields up to 45 T. Fig. 2a presents the Hall resistance as a function of gate voltage for a typical 5-SL Type S device (Device S1) under magnetic fields ranging from 15 T (blue) to 42 T (red). Prominent Hall plateaus appear at $h/\nu e^2$, where $\nu = +1, -1, -2, -3$, and -4 are integer filling factors in the usual quantum Hall language, accompanied by corresponding minima in R_{xx} (Fig. 2b). Among our observed quantized states, the $\nu = -1$ state is recognized as a QAH state adiabatically connected to the QAH state at zero magnetic field (Fig. 1e). Measurements at elevated temperatures reveal a large, field-dependent excitation gap for the $\nu = -1$ and $\nu = -2$ states, on the order of 100 K—significantly larger than the QAH gap obtained in Type A devices. Finite excitation gaps are also observed at higher filling factors. These findings corroborate the enhanced mobility of Type S devices in the FM state.

These quantized states are further resolved as plateaus in the gate-voltage-dependent Hall conductivity σ_{xy} shown in Fig. 2c. The σ_{xy} plots additionally reveal an intriguing fractional state (FS) between $\nu = -2$ and $\nu = -3$, which emerges above a threshold magnetic field of 40 T (Fig. 2c, dashed box); closer examination under fields up to 45 T confirms the existence of this state (Fig. 2c upper inset). While the precise nature of this novel fractional state remains unclear, its observation highlights the increasingly significant role of many-body interactions in higher-quality devices.

Fig. 3a displays the longitudinal conductivity σ_{xx} as a function of both back-gate voltage V_g and magnetic field $\mu_0 H$, illustrating the intricate topological phases in 5-SL MnBi₂Te₄. These phases manifest as regions of minimum σ_{xx} (with quantized σ_{xy} , not shown) separated by sharp boundaries. The phase boundaries correspond to LLs in the conventional quantum Hall framework, where electron levels exhibit positive slopes and hole levels exhibit negative slopes, forming the characteristic Landau fan diagram. These LLs are more clearly resolved in the first derivative of σ_{xy} , $\partial\sigma_{xy}/\partial V_g$, plotted against both V_g and $\mu_0 H$ in Fig. 3b. This derivative plot distinctly resolves the fractional topological phase between the $\nu = -2$ and $\nu = -3$ phases, and uncovers additional topological states at $\nu = -6$ and -8 . These higher filling factors are determined from nearly quantized σ_{xy} .

The Landau fan diagram of the 5-SL MnBi₂Te₄ resembles that of a conventional ambipolar 2D system hosting both electron and hole LLs. However, closer inspection of Fig. 3a reveals major deviations: the lowest levels around the CNP (L_0 , L_1 and L_2) do not converge to a single point at zero magnetic field, and one level (L_2) intersects multiple other LLs with higher filling factors.

How can we understand this unconventional Landau fan diagram? Important insights arise from analyzing the electronic structure of a thin slab of hypothetical FM MnBi₂Te₄. Since FM MnBi₂Te₄ is theorized to be a Weyl semimetal^{2,4}, a thin slab effectively acts as a 2D quantum well of such a semimetal. Fig. 3c illustrates the calculated Γ -point energies of sub-bands formed in this 2D quantum well as slab thickness is varied. When the thickness exceeds 2 SLs, an inversion of the surface bands transitions the system from a $C = 0$ trivial insulator into a $C = -1$ QAH insulator. As the thickness increases further, electron and hole bulk bands begin to populate the QAH gap. In a 5-SL slab, three bulk bands (E_1^e , E_1^h and E_2^h , where the superscript

e and h denote electron and hole band, respectively; Fig. 3c) emerge between the pair of surface bands (E_s^e and E_s^h), effectively reducing the QAH gap from 88 meV to 39 meV, the energy gap between the E_1^e and E_1^h sub-bands.

A finite magnetic field collapses each of these sub-bands into a set of discrete LLs. Fig. 3e presents the calculated energy spectra of these LLs as they evolve with increasing magnetic field. At 45 T, the lowest three LLs are identified as the first LLs of three distinct sub-bands: L_0 originates from the hole sub-band $E_{1,k}^h$, while L_1 and L_2 derive from the electron bands $E_{1,k}^e$ and $E_{2,k}^e$, respectively (Fig. 3e, right panel). Notably, the L_2 level intersects with other LLs at intermediate magnetic fields. These findings provide a compelling explanation for the outstanding features observed in the LL fan diagrams shown in Fig. 3a and 3b. Indeed, density of states (DOS) simulations based on calculated spectra reproduce a fan diagram that closely aligns with the experimental results in Fig. 3b, once level broadening and impurity states are taken into account (Fig. 3d).

With the phase boundaries clarified, we now turn to the topological nature of these phases. Generally, when an external magnetic field is applied, the nontrivial topology of a QAH insulator becomes encoded in its discrete LLs. This QAH topology is fundamentally tied to the parity anomaly of Dirac fermion in $2 + 1$ dimensions^{16,15,17}. The LL-resolved topological phase diagram of 5-SL MnBi₂Te₄ thus provides a unique opportunity for probing this anomaly under a quantizing magnetic field^{18,19}.

We begin with a phenomenological description of the topological phases. At the CNP, a QAH insulator is characterized by a nontrivial Chern number C_0 (for 5-SL MnBi₂Te₄, $C_0 = -1$ by definition) under zero magnetic field. Our experiments on 5-SL MnBi₂Te₄ show that the QAH gap remains open under finite magnetic fields (Fig. 1e). This observation implies that the same C_0 , through adiabatic continuity, continues to describe the QAH phase in the presence of LLs. Since each LL carries a Chern number of -1 , the system's total Chern number decreases by -1 (or increases by $+1$) each time the Fermi level crosses an initially unoccupied (or occupied) LL. Consequently, the topological phases of the system at finite doping are characterized by the topological number $N = C_0 - \Delta N_+ + \Delta N_-$, where ΔN_+ (ΔN_-) represents the number of initially unoccupied (occupied) levels that the Fermi level traversed from the CNP. This topological number, N , as labeled on the phase diagram in Fig. 3d, accurately describes the quantized Hall conductivity, $\sigma_{xy} = Ne^2/h$, observed in these phases.

A deeper understanding of the topological phases invokes the parity anomaly of Dirac fermion in $2 + 1$ dimensions. This anomaly reflects the intrinsic conflict between time-reversal symmetry and gauge invariance when regularizing the Dirac fermion theory in $2 + 1$ dimensions¹⁷. In QAH systems such as 5-SL MnBi₂Te₄, the appropriate regularization scheme breaks time-reversal symmetry while preserving gauge symmetry¹⁷. Under this scheme, the parity anomaly manifests as a topological quantity known as the spectral asymmetry η , which quantifies the asymmetry of the entire spectrum^{18,19}. In the presence of LLs with uniform degeneracy, η corresponds to the imbalance between the total number of unoccupied and occupied LLs. This understanding allows the topological number N to be reformulated as a generalized topological index:

$$N = \frac{N_+ - N_-}{2},$$

where N_+ (N_-) is the total number of unoccupied (occupied) LLs. Comparing this expression to the earlier definition of N yields $N_- = N_+ - 2C_0$ at the QAH gap, a universal relation that

encapsulates the parity anomaly for all QAH systems under external magnetic fields.

In 5-SL MnBi₂Te₄, this relation implies that, counted from the QAH gap, the occupied LLs outnumber the unoccupied LLs by 2. (The fact that these LLs originate from different subbands in 5-SL MnBi₂Te₄ does not affect the analysis.) Compared with a topologically trivial insulator, where $N_- = N_+$, the QAH topology (i.e., the parity anomaly) of 5-SL MnBi₂Te₄ can be viewed as an electron LL inverted to the hole side. Indeed, our calculations identify an anomalous LL—the first LL of the surface band $E_{s,k}^h$, as shown in Fig. 3e—that is responsible for the $\nu = -1$ QAH effect observed in 5-SL MnBi₂Te₄. This anomalous LL, although originating from a hole band, disperses as an electron level all the way to the $\mu_0 H \rightarrow \infty$ limit (Supplementary Fig. 6). So, unlike other hole LLs, this singular level curls upwards from below and crosses the Fermi level at the sample boundary. The resulting chiral edge state gives rise to the quantized QAH conductance that we observe experimentally at $\nu = -1$. This and the other quantized topological states in MnBi₂Te₄, therefore, go far beyond a simple superposition of quantum Hall and QAH effects⁷, and are fundamentally distinct from the 2D Dirac cone models proposed in ref.⁶¹.

Our calculations further predict exotic edge transport in the $\nu = 0$ phase. A schematic of the anticipated LL structure in this phase is presented in Fig. 4b. The upward-dispersing anomalous LL intersects a downward-dispersing normal hole level (the first LL of the $E_{1,k}^h$ sub-band) at the edges. The level crossings create two counter-propagating edge channels on both sides of the specimen, resembling the scenario in a quantum spin Hall insulator^{62–64}. The backscattering and localization likely opens a transport gap at their crossing points^{65,66}, dividing the transport into three regimes, referred to as 0^- , $0'$, and 0^+ , as the Fermi level shifts through the $\nu = 0$ phase. The edge channels in these regimes are illustrated in Fig. 4c. Remarkably, three distinct regions, attributable to the 0^- , $0'$, and 0^+ regimes, are evident in both σ_{xx} and σ_{xy} as the gate voltage sweeps through the $\nu = 0$ phase. These regimes are even more distinctly resolved in the phase diagrams in Fig. 3a and 3b, where sharp boundaries separate the three regimes. These findings provide additional support for our understanding of the topologically nontrivial electronic structure of 5-SL MnBi₂Te₄.

To conclude, we have fabricated devices of intrinsic magnetic topological insulator MnBi₂Te₄ with much improved quality. The advancement enables better QAH quantization at zero magnetic field. More importantly, the high-quality samples produce a rich set of quantized topological states under high magnetic fields, uncovering fundamental links between parity anomaly, anomalous LL structure, and QAH topology. With this longstanding challenge in MnBi₂Te₄ research now overcome, we anticipate that this material will serve as a major playground for exploring novel topological quantum physics.

Reference

1. Otrokov, M. M. *et al.* Unique Thickness-Dependent Properties of the van der Waals Interlayer Antiferromagnet MnBi₂Te₄ Films. *Phys. Rev. Lett.* **122**, 107202 (2019).
2. Zhang, D. *et al.* Topological Axion States in the Magnetic Insulator MnBi₂Te₄ with the Quantized Magnetoelectric Effect. *Phys. Rev. Lett.* **122**, 206401 (2019).
3. Gong, Y. *et al.* Experimental Realization of an Intrinsic Magnetic Topological Insulator. *Chin. Phys. Lett.* **36**, 76801–076801 (2019).
4. Li, J. *et al.* Intrinsic magnetic topological insulators in van der Waals layered MnBi₂Te₄-family materials. *Sci. Adv.* **5**, eaaw5685 (2019).

5. Aliev, Z. S. *et al.* Novel ternary layered manganese bismuth tellurides of the MnTe-Bi₂Te₃ system: Synthesis and crystal structure. *J. Alloys Compd.* **789**, 443–450 (2019).
6. Otrokov, M. M. *et al.* Prediction and observation of an antiferromagnetic topological insulator. *Nature* **576**, 416–422 (2019).
7. Deng, Y. *et al.* Quantum anomalous Hall effect in intrinsic magnetic topological insulator MnBi₂Te₄. *Science* **367**, 895–900 (2020).
8. Liu, C. *et al.* Robust axion insulator and Chern insulator phases in a two-dimensional antiferromagnetic topological insulator. *Nat. Mater.* **19**, 522–527 (2020).
9. Ge, J. *et al.* High-Chern-number and high-temperature quantum Hall effect without Landau levels. *Natl. Sci. Rev.* **7**, 1280–1287 (2020).
10. Gao, A. *et al.* Layer Hall effect in a 2D topological axion antiferromagnet. *Nature* **595**, 521–525 (2021).
11. Gao, A. *et al.* Quantum metric nonlinear Hall effect in a topological antiferromagnetic heterostructure. *Science* **381**, 181–186 (2023).
12. Wang, N. *et al.* Quantum-metric-induced nonlinear transport in a topological antiferromagnet. *Nature* **621**, 487–492 (2023).
13. Qiu, J.-X. *et al.* Observation of the axion quasiparticle in 2D MnBi₂Te₄. *Nature* **641**, 62–69 (2025).
14. Li, S. *et al.* Progress on the antiferromagnetic topological insulator MnBi₂Te₄. *Natl. Sci. Rev.* **11**, nwac296 (2024).
15. Haldane, F. D. M. Model for a Quantum Hall Effect without Landau Levels: Condensed-Matter Realization of the Parity. *Phys. Rev. Lett.* **61**, 2077–2080 (1988).
16. Niemi, A. J. & Semenoff, G. W. Axial-Anomaly-Induced Fermion Fractionization and Effective Gauge-Theory Actions in Odd-Dimensional Space-Times. *Phys. Rev. Lett.* **51**, 2077–2080 (1983).
17. Lapa, M. F. Parity anomaly from the Hamiltonian point of view. *Phys. Rev. B* **99**, 235144 (2019).
18. Böttcher, J., Tutschku, C. & Hankiewicz, E. M. Fate of quantum anomalous Hall effect in the presence of external magnetic fields and particle-hole asymmetry. *Phys. Rev. B* **101**, 195433 (2020).
19. Böttcher, J., Tutschku, C., Molenkamp, L. W. & Hankiewicz, E. M. Survival of the Quantum Anomalous Hall Effect in Orbital Magnetic Fields as a Consequence of the Parity Anomaly. *Phys. Rev. Lett.* **123**, 226602 (2019).
20. von Klitzing, K. The quantized Hall effect. *Rev. Mod. Phys.* **58**, 519–531 (1986).
21. Chang, C.-Z. *et al.* Experimental Observation of the Quantum Anomalous Hall Effect in a Magnetic Topological Insulator. *Science* **340**, 167–170 (2013).
22. Checkelsky, J. G. *et al.* Trajectory of the anomalous Hall effect towards the quantized state in a ferromagnetic topological insulator. *Nat. Phys.* **10**, 731–736 (2014).
23. Kou, X. *et al.* Scale-Invariant Quantum Anomalous Hall Effect in Magnetic Topological Insulators beyond the Two-Dimensional Limit. *Phys. Rev. Lett.* **113**, 137201 (2014).
24. Chang, C.-Z. *et al.* High-precision realization of robust quantum anomalous Hall state in a hard ferromagnetic topological insulator. *Nat. Mater.* **14**, 473–477 (2015).
25. Mogi, M. *et al.* Magnetic modulation doping in topological insulators toward higher-temperature quantum anomalous Hall effect. *Appl. Phys. Lett.* **107**, 182401 (2015).

26. Götz, M. *et al.* Precision measurement of the quantized anomalous Hall resistance at zero magnetic field. *Appl. Phys. Lett.* **112**, 072102 (2018).
27. Fox, E. J. *et al.* Part-per-million quantization and current-induced breakdown of the quantum anomalous Hall effect. *Phys. Rev. B* **98**, 075145 (2018).
28. Okazaki, Y. *et al.* Precise resistance measurement of quantum anomalous Hall effect in magnetic heterostructure film of topological insulator. *Appl. Phys. Lett.* **116**, 143101 (2020).
29. Okazaki, Y. *et al.* Quantum anomalous Hall effect with a permanent magnet defines a quantum resistance standard. *Nat. Phys.* **18**, 25–29 (2022).
30. Rodenbach, L. K. *et al.* Realization of the quantum ampere using the quantum anomalous Hall and Josephson effects. arXiv.2308.00200 (2023).
31. Patel, D. K. *et al.* A zero external magnetic field quantum standard of resistance at the 10–9 level. *Nat. Electron.* **7**, 1111–1116 (2024).
32. Tokura, Y., Yasuda, K. & Tsukazaki, A. Magnetic topological insulators. *Nat. Rev. Phys.* **1**, 126–143 (2019).
33. Liu, C.-X., Zhang, S.-C. & Qi, X.-L. The Quantum Anomalous Hall Effect: Theory and Experiment. *Annu. Rev. Condens. Matter Phys.* **7**, 301–321 (2016).
34. Chang, C.-Z., Liu, C.-X. & MacDonald, A. H. Colloquium: Quantum anomalous Hall effect. *Rev. Mod. Phys.* **95**, 011002 (2023).
35. Chung, S. B., Qi, X.-L., Maciejko, J. & Zhang, S.-C. Conductance and noise signatures of Majorana backscattering. *Phys. Rev. B* **83**, 100512 (2011).
36. Akhmerov, A. R., Nilsson, J. & Beenakker, C. W. J. Electrically Detected Interferometry of Majorana Fermions in a Topological Insulator. *Phys. Rev. Lett.* **102**, 216404 (2009).
37. Fu, L. & Kane, C. L. Probing Neutral Majorana Fermion Edge Modes with Charge Transport. *Phys. Rev. Lett.* **102**, 216403 (2009).
38. Wang, J., Zhou, Q., Lian, B. & Zhang, S.-C. Chiral topological superconductor and half-integer conductance plateau from quantum anomalous Hall plateau transition. *Phys. Rev. B* **92**, 064520 (2015).
39. Lian, B., Sun, X.-Q., Vaezi, A., Qi, X.-L. & Zhang, S.-C. Topological quantum computation based on chiral Majorana fermions. *Proc. Natl. Acad. Sci.* **115**, 10938–10942 (2018).
40. Serlin, M. *et al.* Intrinsic quantized anomalous Hall effect in a moiré heterostructure. *Science* **367**, 900–903 (2020).
41. Li, T. *et al.* Quantum anomalous Hall effect from intertwined moiré bands. *Nature* **600**, 641–646 (2021).
42. Park, H. *et al.* Observation of fractionally quantized anomalous Hall effect. *Nature* **622**, 74–79 (2023).
43. Xu, F. *et al.* Observation of Integer and Fractional Quantum Anomalous Hall Effects in Twisted Bilayer MoTe₂. *Phys. Rev. X* **13**, 031037 (2023).
44. Chen, G. *et al.* Tunable correlated Chern insulator and ferromagnetism in a moiré superlattice. *Nature* **579**, 56–61 (2020).
45. Han, T. *et al.* Large quantum anomalous Hall effect in spin-orbit proximitized rhombohedral graphene. *Science* **384**, 647–651 (2024).
46. Lu, Z. *et al.* Fractional quantum anomalous Hall effect in multilayer graphene. *Nature* **626**, 759–764 (2024).
47. Lian, Z. *et al.* Antiferromagnetic quantum anomalous Hall effect under spin flips and flops.

- Nature* **641**, 70–75 (2025).
48. Li, Y. *et al.* Reentrant quantum anomalous Hall effect in molecular beam epitaxy-grown MnBi₂Te₄ thin films. *arXiv:2401.11450* (2024).
 49. Wang, Y. *et al.* Towards the Quantized Anomalous Hall effect in AlO_x-capped MnBi₂Te₄. *Nat. Commun.* **16**, 1727 (2025).
 50. Deng, Y. *et al.* Gate-tunable room-temperature ferromagnetism in two-dimensional Fe₃GeTe₂. *Nature* **563**, 94–99 (2018).
 51. Hou, F. *et al.* Te-Vacancy-Induced Surface Collapse and Reconstruction in Antiferromagnetic Topological Insulator MnBi₂Te₄. *ACS Nano* **14**, 11262–11272 (2020).
 52. Liu, C. *et al.* Magnetic-field-induced robust zero Hall plateau state in MnBi₂Te₄ Chern insulator. *Nat. Commun.* **12**, 4647 (2021).
 53. Yang, S. *et al.* Odd-Even Layer-Number Effect and Layer-Dependent Magnetic Phase Diagrams in MnBi₂Te₄. *Phys. Rev. X* **11**, 011003 (2021).
 54. Ovchinnikov, D. *et al.* Intertwined Topological and Magnetic Orders in Atomically Thin Chern Insulator MnBi₂Te₄. *Nano Lett.* **21**, 2544–2550 (2021).
 55. Lei, C. *et al.* Metamagnetism of few-layer topological antiferromagnets. *Phys. Rev. Mater.* **5**, 064201 (2021).
 56. Ying, Z. *et al.* Experimental evidence for dissipationless transport of the chiral edge state of the high-field Chern insulator in MnBi₂Te₄ nanodevices. *Phys. Rev. B* **105**, 085412 (2022).
 57. Liu, C. *et al.* Robust axion insulator and Chern insulator phases in a two-dimensional antiferromagnetic topological insulator. *Nat. Mater.* **19**, 522–527 (2020).
 58. Cai, J. *et al.* Electric control of a canted-antiferromagnetic Chern insulator. *Nat. Commun.* **13**, 1668 (2022).
 59. Lai, Y., Ke, L., Yan, J., McDonald, R. D. & McQueeney, R. J. Defect-driven ferrimagnetism and hidden magnetization in MnBi₂Te₄. *Phys. Rev. B* **103**, 184429 (2021).
 60. Garnica, M. *et al.* Native point defects and their implications for the Dirac point gap at MnBi₂Te₄(0001). *npj Quantum Mater.* **7**, 1–9 (2022).
 61. Chong, S. K. *et al.* Anomalous Landau quantization in intrinsic magnetic topological insulators. *Nat. Commun.* **14**, 4805 (2023).
 62. Kane, C. L. & Mele, E. J. Quantum Spin Hall Effect in Graphene. *Phys. Rev. Lett.* **95**, 226801 (2005).
 63. Bernevig, B. A., Hughes, T. L. & Zhang, S.-C. Quantum Spin Hall Effect and Topological Phase Transition in HgTe Quantum Wells. *Science* **314**, 1757–1761 (2006).
 64. Bernevig, B. A. & Zhang, S.-C. Quantum Spin Hall Effect. *Phys. Rev. Lett.* **96**, 106802 (2006).
 65. Maciejko, J., Qi, X.-L. & Zhang, S.-C. Magnetoconductance of the quantum spin Hall state. *Phys. Rev. B* **82**, 155310 (2010).
 66. Essert, S. & Richter, K. Magnetotransport in disordered two-dimensional topological insulators: signatures of charge puddles. *2D Mater.* **2**, 024005 (2015).

Acknowledgements

We thank Philip Kim, Xiaofeng Jin, Yizheng Wu, Dung-Hai Lee, Taige Wang, Zhiqiang Gao, Raquel Queiroz and Yijun Yu for helpful discussions. Part of the sample fabrication was

performed at Nano-fabrication Laboratory at Fudan University. A portion of this work was performed at High Magnetic Field Laboratory, HFIPS, Chinese Academy of Sciences, Hefei, China. Z.G., J.G., Z.H., D.Y., M.L., W.R., and Y.Z. acknowledge support from National Key R&D Program of China (grant no. 2022YFA1403301), National Science Foundation of China (grant no. 1235000130), Innovation Program for Quantum Science and Technology (grant no. 2024ZD0300104), and Shanghai Municipal Science and Technology Commission (grant nos. 23JC1400600 and 2019SHZDZX01). W.R. acknowledges support from National Science Foundation of China (grant no. 12350401) and Shanghai Science and Technology Development Funds (grant no. 22QA1400600). W.R. and H. J. acknowledges support from National Science Foundation of China (grant no. 12350401). J.G. acknowledges support from the National Natural Science Foundation of China (grant no. 12204115) and China Postdoctoral Science Foundation (grant no. 2022M720812). D.Y. acknowledges support from the National Natural Science Foundation of China (grant no. 12004075) and China Postdoctoral Science Foundation (grant no. BX20190084 and 2019M661330). G.H. and C.Z. acknowledge support from National Science Foundation of China (grant no. 62171136). Z.L. and J.W. acknowledge support from National Key R&D Program of China (grant nos. 2019YFA0308404), National Science Foundation of China (grant nos. 12350404, 12174066), Shanghai Municipal Science and Technology Commission (grant no. 23JC1400600, 2019SHZDZX01). C.X. and G.K. acknowledge support from Systematic Fundamental Research Program Leveraging Major Scientific and Technological Infrastructure, Chinese Academy of Sciences under contract no. JZHKYPT-2021-08. Y.S. acknowledges support from National Key R&D Program of China (grant no. 2021YFA1600201), National Science Foundation of China (grant no. 12274412). This work has been supported by the New Cornerstone Science Foundation through the New Cornerstone Investigator Program and the XPLORER PRIZE.

Contributions

Y.Z., W.R., J.W., and X.H.C. supervised the project. J.G. and Z.G. grew the bulk crystals, with assistance from M.S. and Z.X. Z.G. and J.G. fabricated few-layer devices and conducted transport measurements. Z.H. carried out the STM measurements. Z.G., J.G., and D.Y. performed high-field transport measurements at HFIPS, with support from C.X. and G.K. S.W. (Shuang Wu), X.C., and S.W. (Shiwei Wu) performed RMCD measurements. G.H. and C.Z. performed TEM measurements. Z.G., J.G., D.Y., Z.L., J.W., W.R., and Y.Z. analyzed the data. Z.L., H.J., X.C.X., and J.W. performed theoretical calculations. Z.G., W.R., and Y.Z. wrote the manuscript, with input from all authors.

Figures

Figure 1 | QAH effect and magnetic transitions in 5-SL MnBi₂Te₄ devices. **a**, Schematic of the device structure in Type A configuration, overlaid with an optical image of Device A1. The fully transparent substrate comprises Al₂O₃/ITO layers supported on a 500- μ m-thick quartz wafer, with the ITO layer serving as a back gate. Contacts for standard four-terminal R_{xx} measurements are marked. Scale bar, 10 μ m. **b**, Temperature dependence of R_{xx} for four representative Type A 5-SL devices. The Néel transition is evident as kinks in R_{xx} at ~ 23.5 K. **c**, R_{yx} (upper panel) and R_{xx} (lower panel) of Device A1 as functions of magnetic field at $T = 1.5$ K. The hallmark QAH effect is characterized by quantized R_{yx} and vanishing R_{xx} at $\mu_0 H = 0$ T. **d**, R_{yx} (upper panel) and R_{xx} (lower panel) of Device A1 as functions of magnetic field at various temperatures. All data in (c) and (d) are acquired at the CNP ($V_{CNP} = -20$ V), with R_{yx} antisymmetrized and R_{xx} symmetrized to eliminate the mixing of the two components. R_{yx} is additionally rescaled to correct for a 1.01% systematic error in our resistance measurements. **e**, QAH excitation gap versus magnetic field for Devices A1 and A2, derived by fitting the Arrhenius plots of temperature-dependent R_{xx} . Shaded regions represent the error bound of the extracted energy gaps. As the magnetic field increases from zero, the sample transitions through four magnetic states: AFM, M3', CAFM, and FM. Insets depict the schematic magnetic configurations of these states. **f**, First derivative of R_{xx} , $\partial R_{xx}/\partial(\mu_0 H)$, as a function of magnetic field and temperature, measured in a 5-SL device in the Type S configuration (Device S1). Below the Néel temperature, the same magnetic states as in (e) appear as distinct regions separated by magnetic transitions. The sample enters the paramagnetic (PM) state above the Néel temperature. Magnetic transitions are marked by colored ticks. The same set of ticks also indicate transitions in (c), (d), (e), and (f).

Figure 2 | Quantized topological states in 5-SL MnBi₂Te₄ under high magnetic fields. **a-b**, Gate-dependent R_{yx} (a) and R_{xx} (b) measured in Device S1 under magnetic fields from 15 T to 42 T at $T = 0.3$ K. Quantized Hall plateaus in R_{yx} are observed at $h/\nu e^2$, where $\nu = +1, -1, -2, -3, -4$ (dashed lines in a). These plateaus are accompanied by vanishing R_{xx} in (b), as highlighted by vertical lines and the associated filling factors ν . **c**, Gate-dependent Hall conductivity σ_{xy} , derived from R_{yx} and R_{xx} in (a) and (b), under various magnetic fields. Quantized plateaus are clearly resolved at filling factors $\nu = +1, -1, -2, -3, -4$ (dashed lines), along with the emergence of a developing plateau at a fractional filling between $\nu = -2$ and $\nu = -3$ (dashed box). Upper inset: Magnified view of the fractional state as it evolves under magnetic fields up to 45 T. Lower inset: Schematic of the device structure in the Type S configuration, overlaid with an optical image of Device S1.

Figure 3 | Topological phase diagram of 5-SL MnBi₂Te₄. **a**, σ_{xx} as a function of gate voltage and magnetic field, measured in Device S1 at $T = 0.3$ K. The topological phases are labeled by their corresponding filling factors $\nu = +1, 0, -1, -2, -3, -4$. $L_0, L_1,$ and L_2 denote the lowest three LLs near the CNP. The $\nu = 0$ phase can be divided into three distinct regimes, separated by sharp boundaries, and labeled as $0^-, 0',$ and 0^+ . **b**, Derivative of the Hall conductivity, $\partial\sigma_{xy}/\partial V_g$, as a function of gate voltage and magnetic field, measured in the same device in (a) at $T = 0.3$ K. In addition to the topological phases observed in (a), additional phases are resolved at $\nu = -6, -8$, along with a fractional phase between $\nu = -2$ and $\nu = -3$ phases. Dashed lines in (a) and (b) serve as guides to the eye. **c**, Calculated Γ -point energies of

sub-bands in a hypothetical 2D quantum well of ferromagnetic MnBi₂Te₄ at zero magnetic field, as a function of the quantum well thickness, d . The inversion of the two surface bands occurs as d exceeds 2-SL, transitioning the system from a trivial insulator ($C = 0$) to a QAH insulator ($C = -1$). As d further increases, bulk bands begin to populate the gap between the surface bands. The Γ -point energies of 5-SL MnBi₂Te₄ are labeled as $E_n^{e/h}$, where e/h indicates electron or hole sub-bands, and $n = s, 1, 2 \dots$ labels the surface and bulk bands. **d**, Simulated DOS based on calculated LL spectra of 5-SL MnBi₂Te₄, incorporating LL broadening and impurity states. Details of the simulation are presented in Fig. S5. **e**, Calculated field-dependent LL spectra (left panel), schematic band structure (middle panel) and high-field LL DOS (right panel) for 5-SL MnBi₂Te₄. Sub-bands are labeled as $E_{n,k}^{e/h}$, where k is the wavevector. The first LL of the $E_{s,k}^h$ sub-band is identified as an anomalous LL—a hole level that disperses like an electron level—responsible for the QAH topology and parity anomaly in 5-SL MnBi₂Te₄ under high magnetic fields (see text).

Fig. 4 | Helical edge transport in the $\nu = 0$ phase. **a**, Gate-dependent σ_{xx} (left panel) and σ_{xy} (right panel) in the $\nu = 0$ phase under high magnetic fields ranging from 32 T to 42 T. Three distinct regimes, labeled as 0^- , $0'$, and 0^+ , are identified within this phase. **b**, Schematic LL structure of a finite 5-SL MnBi₂Te₄ in the $\nu = 0$ phase. The anomalous LL (the first LL of the $E_{s,k}^h$ sub-band, shown in red) intersects with a hole LL (the first LL of the $E_{1,k}^h$ sub-band, shown in blue) at the two edges of the sample, forming two counter-propagating helical edge channels on each edge. Backscattering between the two channels likely induces a hybridization gap at the level crossing. Edge transport is thus divided into three scenarios, corresponding to 0^- , $0'$, and 0^+ , as the Fermi level shift through the $\nu = 0$ gap. **c**, Real-space illustration of the edge transport anticipated in the 0^- , $0'$, and 0^+ regimes. In the 0^- and 0^+ regimes, red and blue lines represent the two counter-propagating chiral edge channels arising from LL crossing in (b). These edge channels are absent in the $0'$ regime.

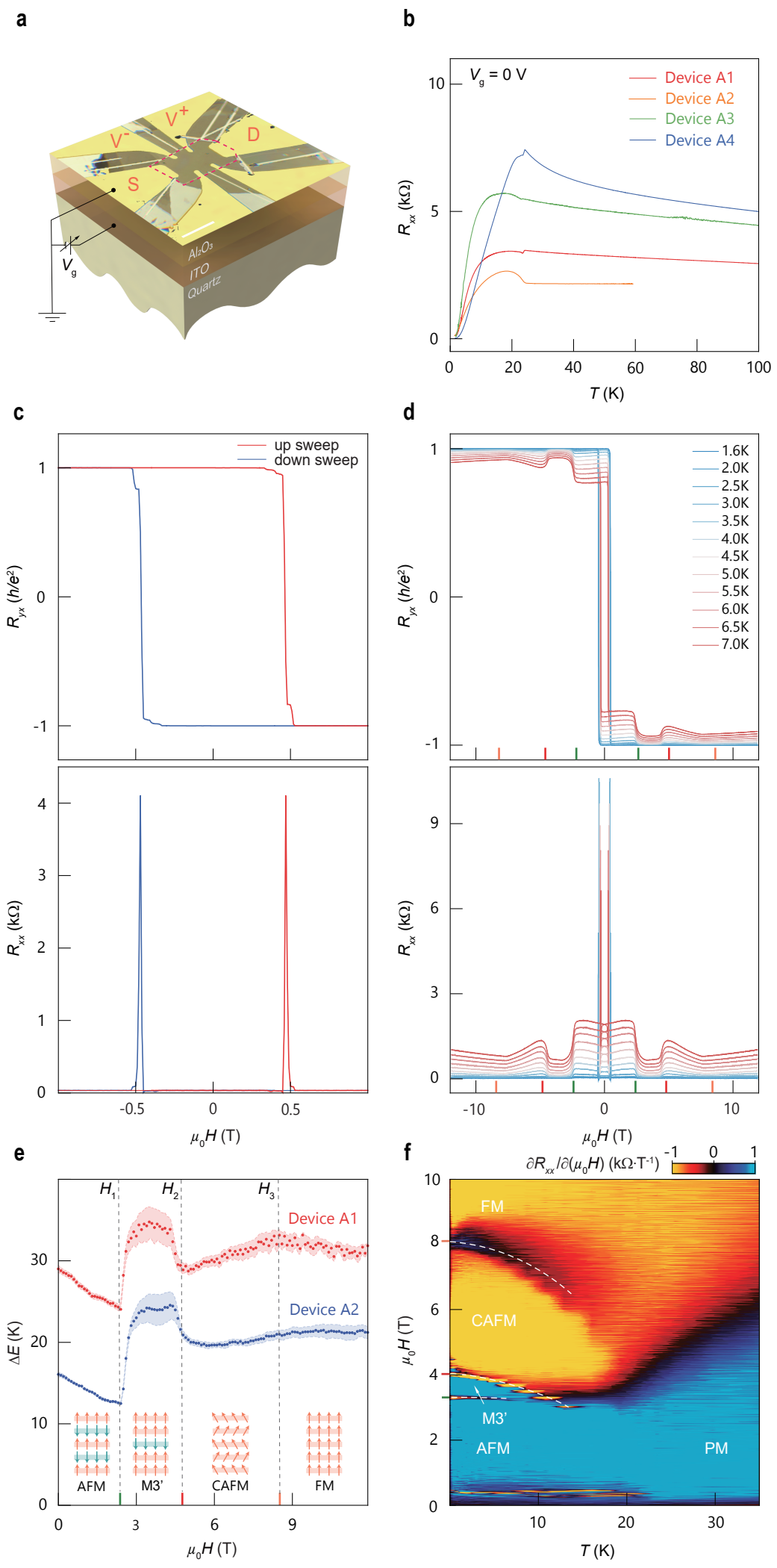


Fig. 1, Z.X. Guo *et al*

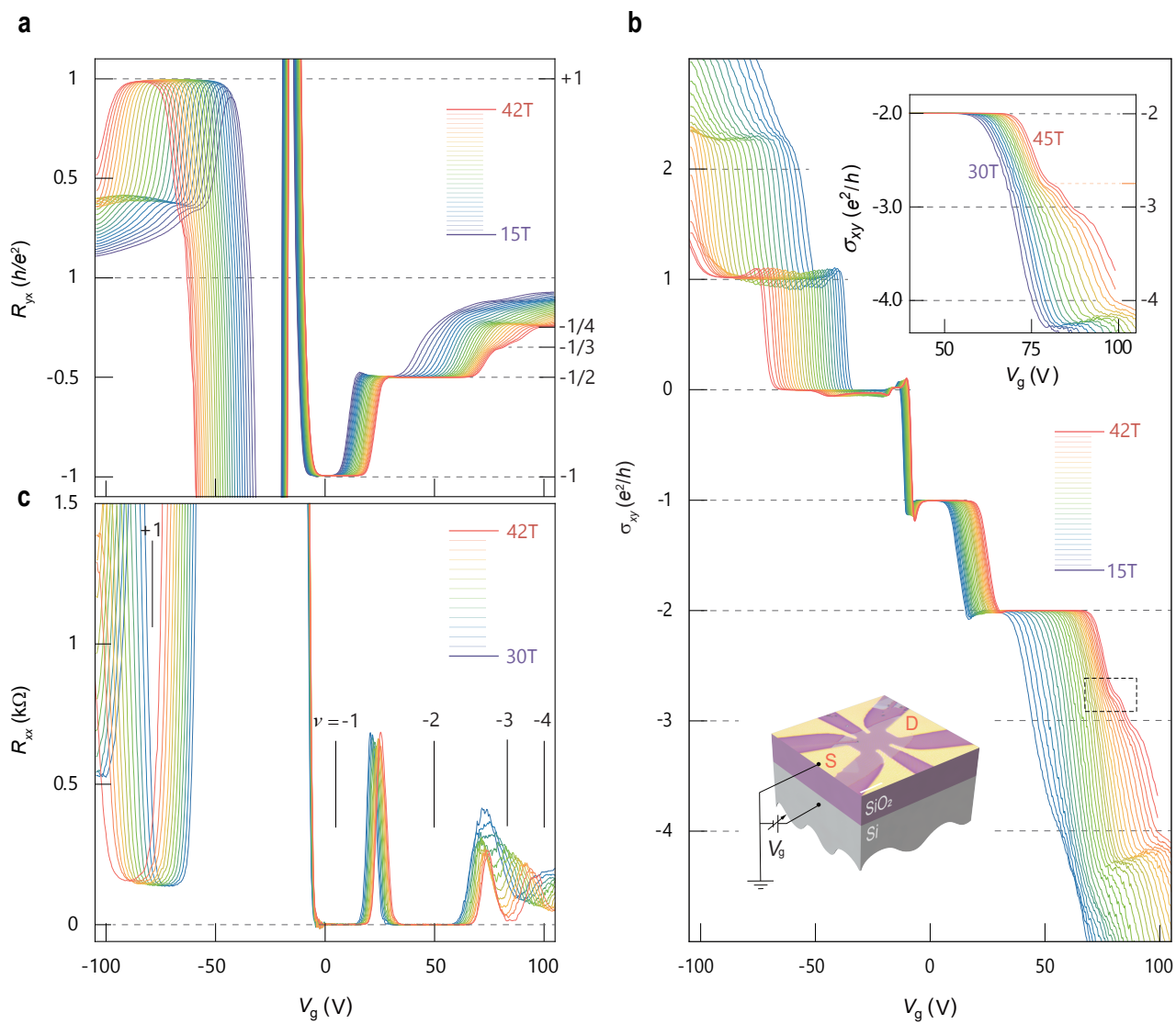


Fig. 2, Z.X. Guo *et al*

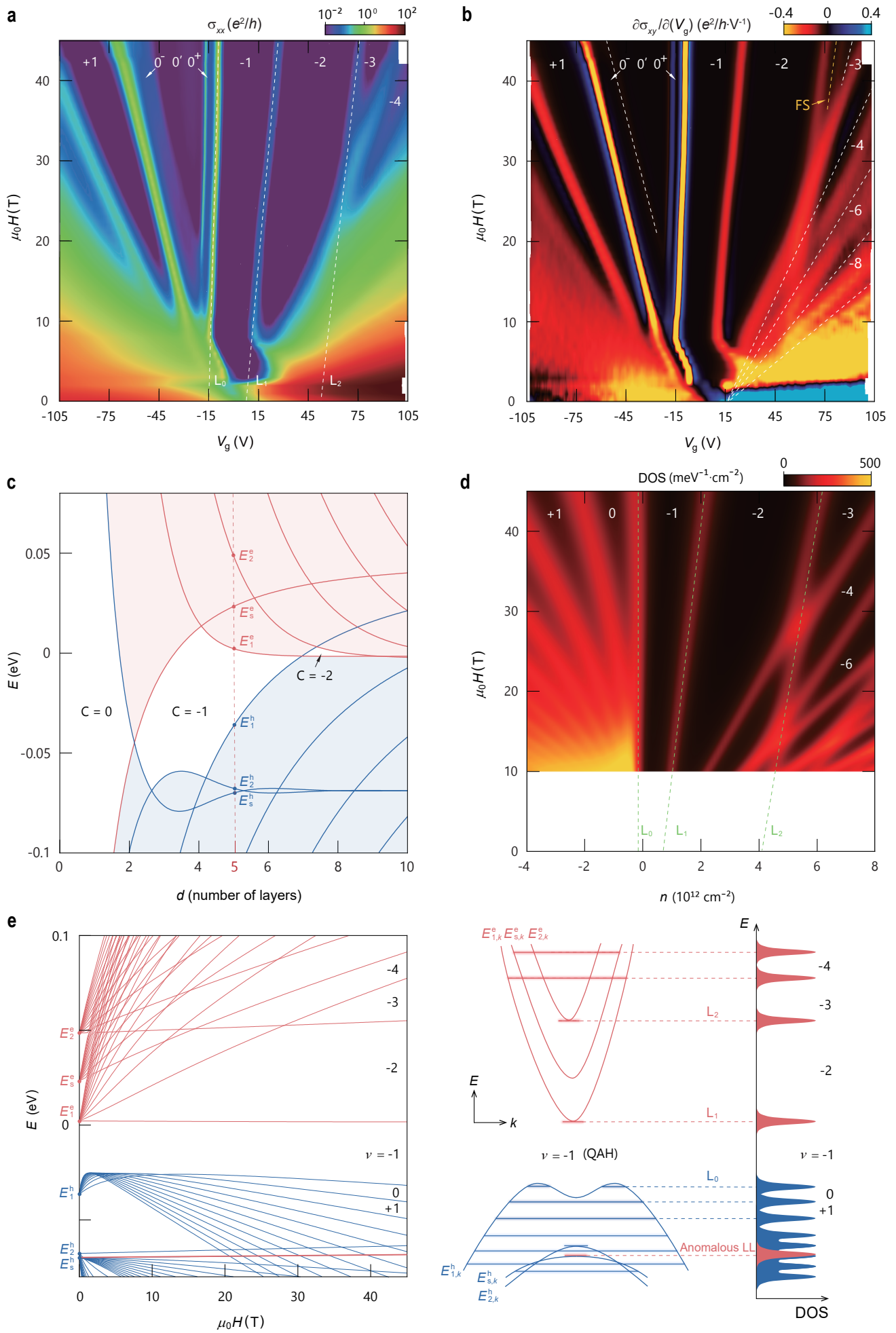


Fig. 3, Z.X. Guo *et al*

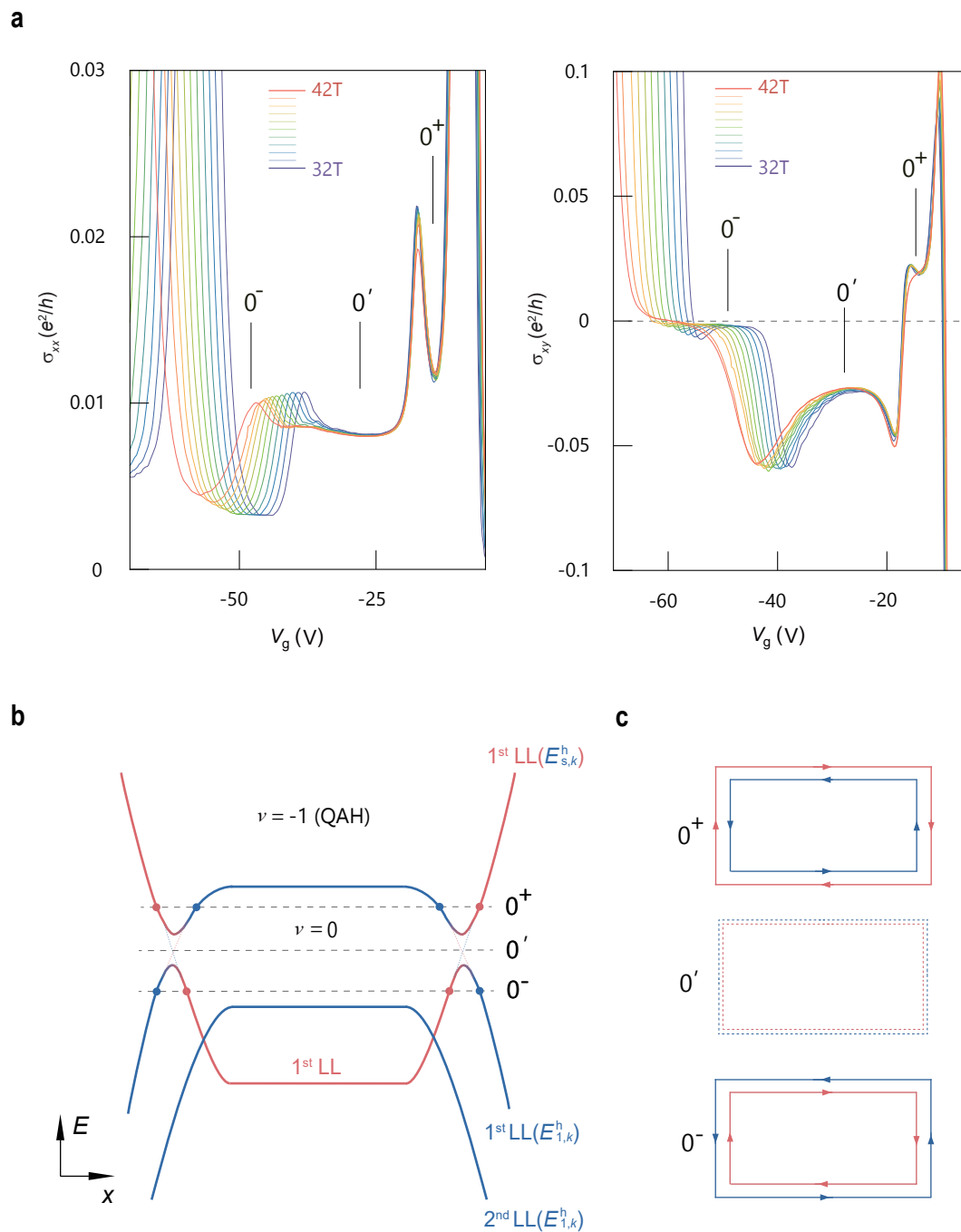


Fig. 4, Z.X. Guo *et al*